Bioactive Materials 41 (2024) 564–576

Contents lists available at ScienceDirect

Bioactive Materials

journal homepage: www.keaipublishing.com/en/journals/bioactive-materials

Zinc finger-inspired peptide-metal-phenolic nanointerface enhances bone-implant integration under bacterial infection microenvironment through immune modulation and osteogenesis promotion

Lin Xu [a,b,1], Jie Fang [a,1], Jiezhou Pan [c], Hexu Qi [a], Yun Yin [c], Yunxiang He [c], Xueqi Gan [d], Yifei Li [e,*], Yu Li [a,**], Junling Guo [c,f,g,h,***]

[a] State Key Laboratory of Oral Diseases, National Center for Stomatology, National Clinical Research Center for Oral Diseases, Department of Orthodontics, West China Hospital of Stomatology, Sichuan University, Chengdu, 610041, China
[b] Key Laboratory of Birth Defects and Related Diseases of Women and Children of MOE, Department of Pediatric Dentistry, West China Second University Hospital, Sichuan University, Chengdu, 610041, China
[c] BMI Center for Biomass Materials and Nanointerfaces, College of Biomass Science and Engineering, Sichuan University, Chengdu, 610065, China
[d] State Key Laboratory of Oral Diseases, National Center for Stomatology, National Clinical Research Center for Oral Diseases, Department of Prosthodontics, West China Hospital of Stomatology, Sichuan University, Chengdu, 610041, China
[e] Key Laboratory of Birth Defects and Related Diseases of Women and Children of MOE, Department of Pediatrics, West China Second University Hospital, Sichuan University, Chengdu, 610041, China
[f] National Engineering Laboratory for Clean Technology of Leather Manufacture, Sichuan University, Chengdu, 610065, China
[g] State Key Laboratory of Polymer Materials Engineering, Sichuan University, Chengdu, 610065, China
[h] Bioproducts Institute, Department of Chemical and Biological Engineering, The University of British Columbia, Vancouver, BC, V6T 1Z4, Canada

ARTICLE INFO

Keywords:
Metal-phenolic network
Implant
Osseointegration
Inflammation
Abaloparatide

ABSTRACT

Orthopedic and dental implantations under bacterial infection microenvironment face significant challenges in achieving high-quality bone-implant integration. Designing implant coatings that incorporate both immune defense and anti-inflammation is difficult in conventional single-functional coatings. We introduce a multi-functional nanointerface using a zinc finger-inspired peptide-metal-phenolic nanocoating, designed to enhance implant osseointegration under such conditions. Abaloparatide (ABL), a second-generation anabolic drug for treating osteoporosis, can be integrated into the design of a zinc-phenolic network constructed on the implant surface (ABL@ZnTA). Importantly, the phenolic-coordinated Zn^{2+} ions in ABL@ZnTA can act as zinc finger motif to co-stabilize the configuration of ABL through multiple molecular interactions, enabling high bioactivity, high loading capacity (1.36 times), and long-term release (>7 days) of ABL. Our results showed that ABL@ZnTA can modulate macrophage polarization from the pro-inflammatory M1 towards the anti-inflammatory M2 phenotype, promoting immune osteogenesis with increased OCN, ALP, and SOD 1 expression. Furthermore, the ABL@ZnTA significantly reduces inflammatory fibrous tissue encapsulation and enhances the long-term stability of the implants, indicated by enhanced binding strength (6 times) and functional connectivity (1.5−3 times) in the rat bone defect model infected by *S. aureus*. Overall, our research offers a nano-enabled synergistic strategy that balances infection defense and osteogenesis promotion in orthopedic and dental implantations.

Peer review under responsibility of KeAi Communications Co., Ltd.
* Corresponding author.
** Corresponding author.
*** Corresponding author. BMI Center for Biomass Materials and Nanointerfaces, College of Biomass Science and Engineering, Sichuan University, Chengdu, 610065, China.
E-mail addresses: liyfwcsh@scu.edu.cn (Y. Li), yuli@scu.edu.cn (Y. Li), junling.guo@ubc.ca, junling.guo@scu.edu.cn (J. Guo).
[1] The authors have contributed equally to this work and share first authorship.

https://doi.org/10.1016/j.bioactmat.2024.08.009
Received 10 May 2024; Received in revised form 22 July 2024; Accepted 12 August 2024

1. Introduction

Implants are commonly used in traumatic orthopedics and denture restoration [1]. However, open fractures and accompanying bacterial infections often hinder the effectiveness of implants in achieving osseointegration. Infection after fracture internal fixation (IAFF), is a possible complication after orthopaedic surgery (ranging from 1 to 2 % for closed fractures and up to 30 % for open fractures) [2–4]. Besides, individuals with severe periodontal disease or apical periodontitis may encounter difficulties of immediate implantation (failure rate increasing 3−5 times) [5–7]. Orthodontic temporary devices have a failure rate of 11–17 %, frequently within the first-month post-implantation, significantly impacting treatment effectiveness and duration [8]. The anti-infective capabilities of implants in different clinical scenarios prove to be crucial [9]. Many strategies have been employed to fabricate smart stimulus-responsive materials for bone therapy and bone regeneration [10–12]. Although previous implant coatings have demonstrated antimicrobial effects [13,14], achieving a delicate balance between immune defense and inflammation suppression remains a significant challenge and complex endeavor [15–18]. Namely, facilitating proper osseointegration necessitates the provision of appropriate, reasoned stimuli for staged bone healing [19–21]. Nevertheless, conventional implant coatings often exhibit only a single antimicrobial or anti-inflammatory function and lack sufficient osteogenic activity. For example, during immediate implant placement following the extraction of teeth affected by severe periodontitis, the buccal threads of implants are frequently exposed without bone coverage, leading to implant loosening and failure [22].

Bioactive molecules, such as osteogenic peptides, miRNAs, and antibodies, are rapidly emerging in the application of bone regeneration due to their excellent osteogenic functions [23–26]. Especially, parathyroid hormone (PTH) and parathyroid hormone-related protein (PTHrP) have been proven to regulate calcium homeostasis, skeletal development, and bone remodeling by activating the parathyroid hormone 1 receptor (PTH1R) [27–29]. As an analog of PTHrP, abaloparatide (ABL) is a peptide containing 34 amino acids that has been approved by the Food and Drug Administration (FDA) for treating osteoporosis as a bone anabolic agent [30]. Although the receptor binding domain (the first 21 amino acids) is identical in both molecules, ABL distinguishes itself through strategic amino acid substitutions occurring between positions 22 and 34 of the PTHrP sequence, acquiring a higher degree of stability [31]. The medication of ABL is a more economical approach, with a price point lower than that of teriparatide (TPTD, PTH 1−34) for the treatment of women at increased risk of fractures [32]. Additionally, ABL has a relatively less propensity to promote bone resorption than TPTD and shows a significantly lower incidence of hypercalcemia [33]. We have previously found that ABL outperforms TPTD in protecting against alveolar bone loss in periodontitis [34], and the bioactive calcium phosphorus nanoflowers loaded with ABL can promote alveolar bone regeneration in the tooth extraction sockets [35]. However, the current use of ABL is generally oral or by subcutaneous injection (the half-life is about an hour or less) [36], which makes it challenging to achieve an effective local concentration at the tissue engineering bone repair interface. Moreover, the structural stability and bioactivity of ABL are highly sensitive to the preparation process and applied microenvironment.

Metal-phenolic networks (MPNs) have emerged as a versatile class of self-assembled supramolecular materials, comprising polyphenol building blocks and metal ions [37,38]. Our group and other researchers have demonstrated that the inherent adherent properties of polyphenols enable MPN deposition onto various materials, allowing for the rational design of functional surfaces [39]. Furthermore, the catechol or galloyl groups of MPNs provide high binding affinity through multiple interactions (e.g., metal coordination, hydrogen bonding, and hydrophobic interaction) with diverse metals, biomacromolecules, membranes, and living cells for functional achievements [40,41]. However, these previous studies have only explored the reversible interactions between polyphenols and bioactive molecules [42], and these relatively weak interactions, mediated by simple non-covalent hydrogen bonds or hydrophobic interaction, result in low loading capacity and non-desirable rapid release from the MPN-functionalized surfaces [43,44].

To overcome the low network robustness and loading efficiency of biotherapeutics, we obtained inspiration from the bionic design of the zinc finger motif. The zinc finger motif, consisting of approximately 30 amino acids in a loop stabilized by Zn^{2+} ion, is a common structural motif in DNA-binding protein [45]. The characteristic motifs of amino acid residues in peptide chains (4 Cys or 2 Cys and 2 His) coordinate with Zn^{II} to stabilize the α-helix structure within the motif. In this study, we introduce an ABL-integrated Zn^{II}-tannic acid (TA)-constructed MPN nanointerface for the multifunctional surface functionalization of bone implants under bacterial infection, denoted as ABL@ZnTA. Given that ABL peptide also possesses characteristic α-helical structures, the MPN-coordinated Zn^{II}, mimicking a zinc finger motif, can maintain the stability of ABL peptide within the Zn-TA nanocoating [46,47], thus enhancing loading capacity and exhibiting excellent antimicrobial performance [48]. In addition, the preservation of structural and functional integrity can be further attributed to the multiple interactions, such as hydrogen bonds, hydrophobic interactions, and ion interactions, between TA and ABL molecules. Importantly, the ABL@ZnTA nanointerface achieves precise modulation of staged osseointegration, enabled by a fine balance between anti-inflammatory and immunomodulation (Fig. 1A). Early macrophage phenotypic modulation and reduction of inflammatory fibrous tissue encapsulation under bacterial infection lead to the restoration of the normal metabolic state, building an optimal osteo-immune microenvironment for direct bone formation at the subsequent contact interface. Collectively, this biomimetically-designed ABL@ZnTA demonstrates as a nano-enabled synergistic and balancing strategy for implant infection defense and osteogenesis promotion in the applications of trauma repair and immediate dental implantation.

2. Materials and methods

2.1. Fabrication of ABL@ZnTA assembly on Ti implants

Commercially pure Ti disks ($\Phi 10 \times 1$ mm^3) were used in this study. The disks were cleaned in acetone, ethanol, and ultrapure water using ultrasound in sequence. Next, the samples were placed in 850 μL of Milli-Q water, followed by adding 50 μL of TA (10 mg/mL) and 100 μL of ABL (10 mg/mL). The resulting mixture, containing ABL, TA, and Ti substrate, was mixed vigorously using a vortex mixer for 5 s, then incubated in an Eppendorf thermomixer at 4 °C and 1400 rpm for 4 h. The above TA-ABL/Ti substrates were then slightly dried and gently rinsed in 1 mL of Zinc sulfate solution ($ZnSO_4$; 0.3 mg/mL), which harvested ABL@ZnTA/Ti substrates.

The surface topography of the substrates was analyzed using a scanning electron microscope (SEM, JEOL JSM-7500 F, Japan). Elemental mapping, including carbon (C), oxygen (O), nitrogen (N), and zinc (Zn) elements, was performed using energy-dispersive X-ray spectrometry (EDS) equipped with the SEM machine. The wettability of various substrates was determined using the water contact angle apparatus (Zhongchen Digital Technic Apparatus Co., Shanghai), with 5 μL RO water in each test. The elemental composition and chemical state of TA-ABL and ABL@ZnTA surfaces were analyzed by Attenuated total reflectance Fourier transform infrared spectroscopy (ATR-FTIR, Spectrum Two, PerkinElmer, USA) and X-ray photoelectron spectroscopy (XPS, AXIS Supra, Kratos, USA). The methodology of release and adhesion behavior and molecular dynamics simulations is described in Supplementary materials.

2.2. In vitro experiment

MC3T3, a murine-derived osteoblast precursor cell line, and

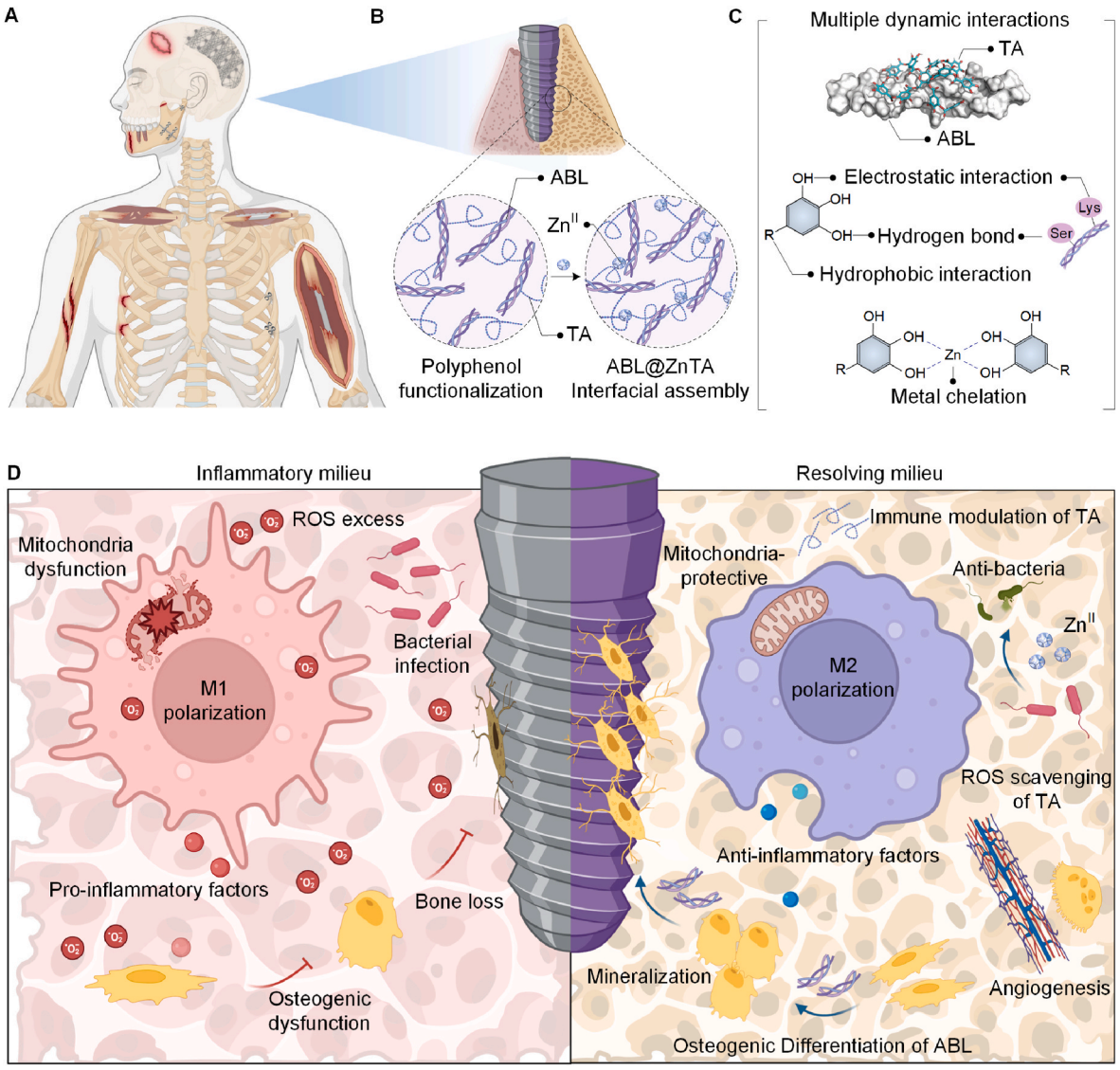

Fig. 1. Schematic illustration for the nanoengineering of the ABL@ZnTA nanointerface. (A) Clinical situations in which functional coatings can be applied, including traumatic fractures and immediate dental implantation in bacterial infection microenvironment. (B) Preparation of the TA-ABL and ABL@ZnTA nanointerfaces on Ti implants. (C) Multiple interactions between TA and ABL, and metal chelation between TA and Zn^{II}. (D) Osseointegration process on clinically used Ti implant through anti-inflammation and immunomodulation against bacterial infection.

RAW264.7 cells, a murine-derived macrophage cell line, were generously provided by the State Key Laboratory of Oral Diseases, West China Hospital of Stomatology. The cells were cultured in Dulbecco's modified Eagle medium (DMEM) (HyClone, USA) supplemented with 10 % fetal bovine serum (Gibco) and 1 % antibiotic solution of penicillin/streptomycin (Gibco) at 37 °C in a humidified incubator with a 5 % CO_2 atmosphere. The cells were passaged through trypsinization once they reached 80 % confluence. The culture media was changed every 2 d. The methodology of compatibility evaluation, immuno-modulatory properties, anti-oxidative and reactive oxygen species (ROS) scavenging capacity, and osteogenic potential are described in Supplementary materials. The cells were treated with 1 μg/mL lipopolysaccharides (LPS) or H_2O_2 (200 μM) to induce inflammatory or excess ROS microenvironment.

2.3. Antibacterial assessment

Staphylococcus aureus (S. aureus) was used in the present study. The preservation solution of *S. aureus* was resuscitated in fresh Luria Broth solution for 18 h while gently shaking at 150 rpm at 37 °C. Subsequently, the *S. aureus* suspension was diluted to 2×10^7 CFU/mL. Then, 40 μL of the diluted bacterial suspension was seeded onto coated Ti substrates (n = 3). The plates were incubated at 37 °C for 24 h. The relative bacterial viability was determined using the agar plate dilution method. The bacterial suspension was diluted 10-fold in LB. 30 μL of bacterial diluent was spread over a solid Luria Broth agar (LBA) plate and cultured at 37 °C overnight. The relative bacterial viability was determined by counting the colony-forming units (CFUs) on LBA plates, which was estimated by calculating the ratio of colony numbers in the experimental group to those in the control group. All assays were performed 3 times.

For morphological Characterization, *S. aureus* suspension was inoculated onto the Ti substrates and cultured overnight. After 24 h of culture, *S. aureus* was fixed with 2.5 % glutaraldehyde at 4 °C overnight. Subsequently, the fixed samples were dehydrated with gradient ethanol (30, 50, 75, 85, 95, and 100 %) for 15 min sequentially. Finally, the bacteria were dried for further observation using SEM.

2.4. In vivo experiment

The animal experiments were approved by the Research Ethics Committee of West China Hospital of Stomatology, Sichuan University, China (No. WCHSIRB-D-2023-362) and performed by the guidelines for animal experimentation of the university/the Animal Research N3CRs guidelines for Reporting of In Vivo Experiments (ARRIVE) guidelines. A total of 36 male Sprague−Dawley rats (7-week-old, 150−170 g each) were purchased from Dashuo (Chengdu, China). The rats were maintained in a specific pathogen-free (SPF) animal facility with a daily 12-h day/night cycle and provided free access to food and water. The sample size was calculated using power analysis, and a minimum of 4 rats was required in each group at each time point (Supplementary materials).

After one week of adaptive feeding, the rats were randomly assigned to 3 groups: the pristine Control group, the TA-ABL group, and the ABL@ZnTA group. The Ti–6Al–4V implants (Φ1.5 × 3 mm, sandblasted and acid-etched) were used in the experiment. All the coated implants were soaked in an *S. aureus* solution (10^6 CFU/mL) for 30 min. The rats were anesthetized by intraperitoneal injection of sodium pentobarbital to ensure analgesia in the surgical site. Following anesthesia, the hind limbs were shaved, and surgical procedures were carried out aseptically. A scalpel made a 10-mm incision on the inside of the knee joint, and then the muscles, patellas, and associated ligaments were uncovered to expose the femoral condyle cartilage. The implant cavity (Φ1.5 mm) was created by a pilot drill of a dental hand-piece with the irrigation of precooled sterilized physiological saline. Then, implants were gently inserted into the drilled holes, and the soft tissues were sutured. To prevent infection after surgery, penicillin (100,000 IU) was administered *via* intramuscular injection. The evaluation of immune response, biomechanical test and bone-to-implant contact, Micro-CT analysis, and histomorphometry were conducted (Supplementary materials).

2.5. Statistical assessment

The data were presented as mean ± SD. Statistical analysis was performed using GraphPad Prism 8.0 software (GraphPad Software, Inc., CA, USA). All experiments were repeated at least 3 times, and representative results were presented. Two-group differences were assessed by Student's *t*-test, while the differences among three or more groups were assessed by one-way analysis of variance (ANOVA) followed by Tukey *posthoc* test for multiple comparisons, as detailed in the respective figure legends. The *P*-values (*<0.05, **<0.01, ***<0.001) indicate significant differences.

3. Results

3.1. Preparation and characterization of the ABL@ZnTA nanointerface

We successfully synthesized ABL@ZnTA nanointerfaces, as confirmed by SEM, EDS mapping, contact angle, and XPS characterizations (Fig. 1B). SEM shows that TA-ABL and ABL@ZnTA coatings form a rougher interface nearly uniformly covered with nanoparticles, which facilitates the recruitment and adhesion of osteoblasts and immune cells (Fig. 2A). Furthermore, Fig. 2B displays the characteristic elemental signals of the surface, particularly the uniform distribution of the Zn element from the MPN structure [49,50], and the presence of ABL peptide is attributed to the N element [51].

Additionally, Fig. 2C illustrates that the TA-ABL and ABL@ZnTA surfaces exhibit more excellent hydrophilicity than the pure Ti surfaces. Fig. 2D shows that the phenolic hydroxyl vibrational band is observed near 1192 cm^{-1}. Additionally, peaks near 1040 and 1450 cm^{-1} correspond to the C–OH vibrational band and the benzene ring framework, respectively, confirming the presence of TA. Polyphenol-peptide interactions alter the conformation of the peptide and induce spectral changes in the amide I band at 1647 cm^{-1} (mainly C=O stretch) and amide II band at 1567 cm^{-1} (C–N stretching coupled with N–H bending modes). Besides, C, N, O, and Zn are detected on the surfaces in the XPS spectra (Fig. 2E and F). Compared to the TA-ABL group, the N:C ratios are higher in the ABL@ZnTA group, indicating more peptides on the surface.

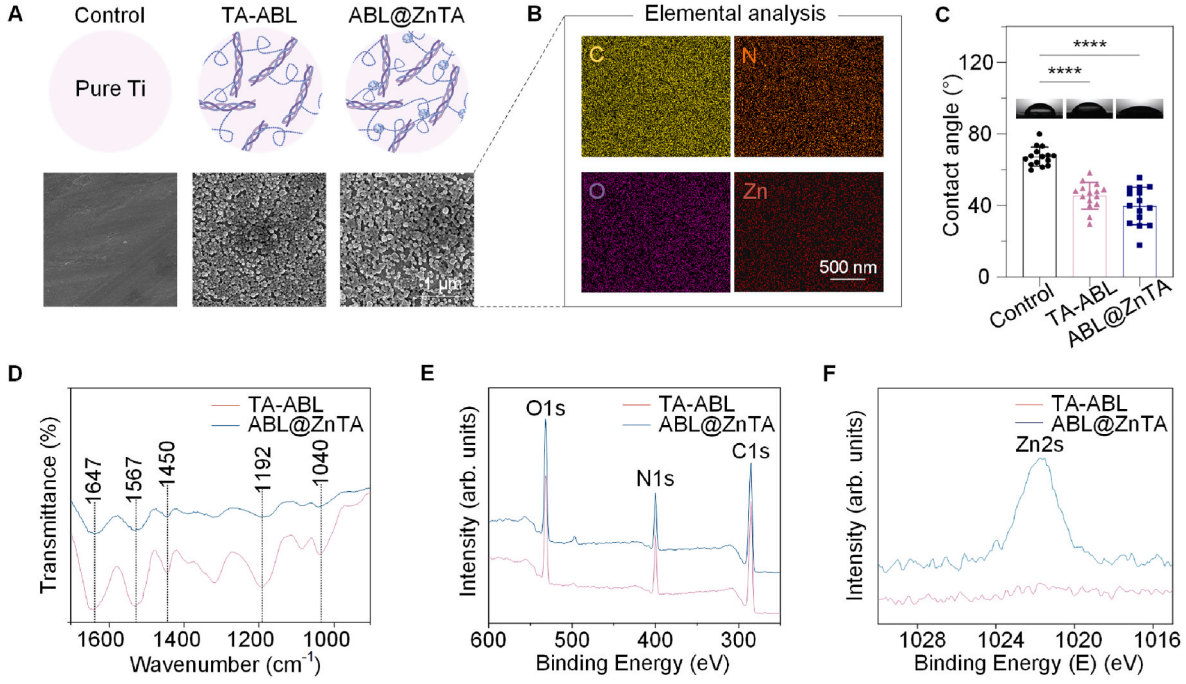

Fig. 2. Characterization of the TA-ABL and ABL@ZnTA nanointerfaces. (A) Micromorphology of the TA-ABL and ABL@ZnTA coatings measured by SEM. (B) EDS including C, N, O, and Zn of the ABL@ZnTA coating. The Zn signal from the elemental analysis indicates the formation of the metal-phenolic network on the ABL@ZnTA nanointerface. (C) Static water contact angle of the sample surfaces. (D) ATR-FTIR of the TA-ABL and ABL@ZnTA surfaces. XPS broad spectra (E) and high-resolution XPS spectra of Zn2s (F) of the TA-ABL and ABL@ZnTA nanointerfaces.

3.2. Sustained release property and molecular mechanism of interactions

Fig. 3A shows that, though the introduction of TA leads to a decrease in peak intensity, the α-helix structure of ABL maintains after the polyphenol functionalization [52]. Both TA-ABL and ABL@ZnTA coatings exhibit long-term release behavior of ABL peptides (Fig. 3B). The cumulated dose of the ABL@ZnTA coating is 1.36 times higher than that of the TA-ABL coating, indicating the ability to anchor and stabilize more peptides, but remained at microdose with no apparent burst release. The loading efficiency of ABL, TA, and Zn^{II} in the ABL@ZnTA group is provided in Fig. S1A, and the coating disassembly is mainly by destroying ionic interaction in Fig. S1B. The remaining coating is still observed at 21 d, especially in the ABL@ZnTA/Ti implant (Fig. 3C). The Young's modulus and hardness of TA-ABL and ABL@ZnTA coatings are shown in Fig. S2, exhibiting similar mechanical strength with cancellous bone around the implant [53].

Fig. 3D shows the multiple dynamic interactions among TA, ABL, and Zn^{II}, indicating many non-covalent bonds, such as electrostatic interaction, hydrogen bond, cation-π, and hydrophobic interaction. Visualization of the simulation trajectory for the docking conformation of TA and ABL is shown in the Supporting Information. When the system reaches equilibration, the TA and ABL molecules are closely overlapped compared to their start states, suggesting that solid interactions have formed between the TA molecule and the ABL peptide (Figs. 1C and 3D). The simulated root mean square deviation (RMSD) is shown in the top right corner of Fig. 3D. RMSD values are stable after 100 ns, indicating that the complex conformation is also stable and the simulation reaches equilibrium. Thus, 100–200 ns simulation trajectories are used for subsequent energy calculation and analysis. The bottom right corner of Fig. 3D shows the absolute value of the Calculation of Receptor-Ligand binding free Energy using the MMPBSA method. The negative ΔTOTAL value indicates that the acceptor ABL peptide and the ligand TA can indeed bind. Fig. 3E shows the representative interactions between TA and ABL peptides. The electrostatic interaction (−136.15 ± 6.94 kcal/mol) and hydrogen bond (−80.98 ± 4.46 kcal/mol) are found to be the two main intermolecular interactions between TA and ABL, which accounts for 93.9 %, demonstrating the robust interactions between phenolic hydroxyl from TA and amide group from ABL peptide. Consequently, the phenolic-coordinated Zn^{II} found in ABL@ZnTA functions similarly to a zinc finger motif, co-stabilizing ABL peptide through various molecular interactions. This synergy facilitates heightened bioactivity, substantial loading capacity, and sustained release of ABL over an extended period.

3.3. Biocompatibility, anti-inflammatory, and immunomodulatory activity

The biocompatibility of the ABL@ZnTA coating was evaluated by initial adhesion activity and cell viability [54]. The confocal laser scanning microscopy (CLSM), SEM, Live/Dead cell staining, and cell counting kit 8 (CCK-8) showed the surfaces show no toxicity to MC3T3 and RAW264.7 cells under the physiology condition (Fig. 4A–C and Fig. S3).

Fig. 4D is a mechanistic map of immunomodulation. The quantitative real-time polymerase chain reaction (qRT-PCR) results reveal that the TA-ABL and ABL@ZnTA coatings decrease the expression of nitric oxide synthase (*iNOS*), tumor necrosis factor-α (*TNF-α*), and interleukin 1β (*IL-1β*) mRNA while promoting the gene expression of interleukin 4

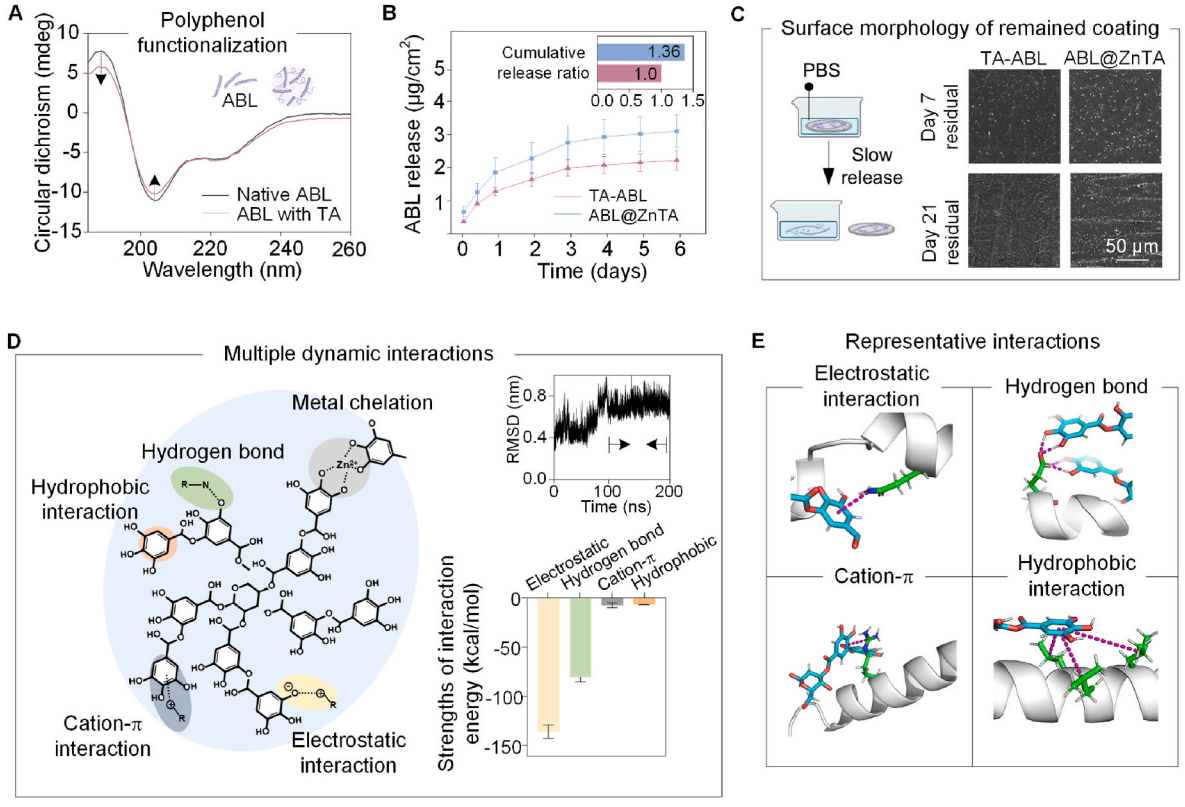

Fig. 3. Sustained release property and molecular mechanism of multiple interactions. (A) Circular dichroism spectroscopy of native ABL and TA-ABL complex. The α-helix structure of the ABL peptide is maintained. (B) Release kinetics of ABL peptide over 6 days in PBS. Both TA-ABL and ABL@ZnTA coatings achieve satisfactory release of ABL, and the accumulated dose of the ABL@ZnTA coating is 1.36 times higher than that of the TA-ABL coating. (C) SEM of the coated Ti samples after soaking in PBS for 7 and 21 days. The remaining coating is still observed, especially in the ABL@ZnTA/Ti implant. (D) Left: Schematic diagram of the multiple dynamic interactions among TA, ABL, and Zn^{II}. Right: RMSD of the simulated trajectory and the absolute value of Calculation of Receptor-Ligand binding free energy of different interactions. (E) Four representative interactions between TA and ABL peptide. To differentiate the various components, the TA molecules, the amide group on ABL (labeled gray), and the interaction forces are marked in blue, green, and violet, respectively.

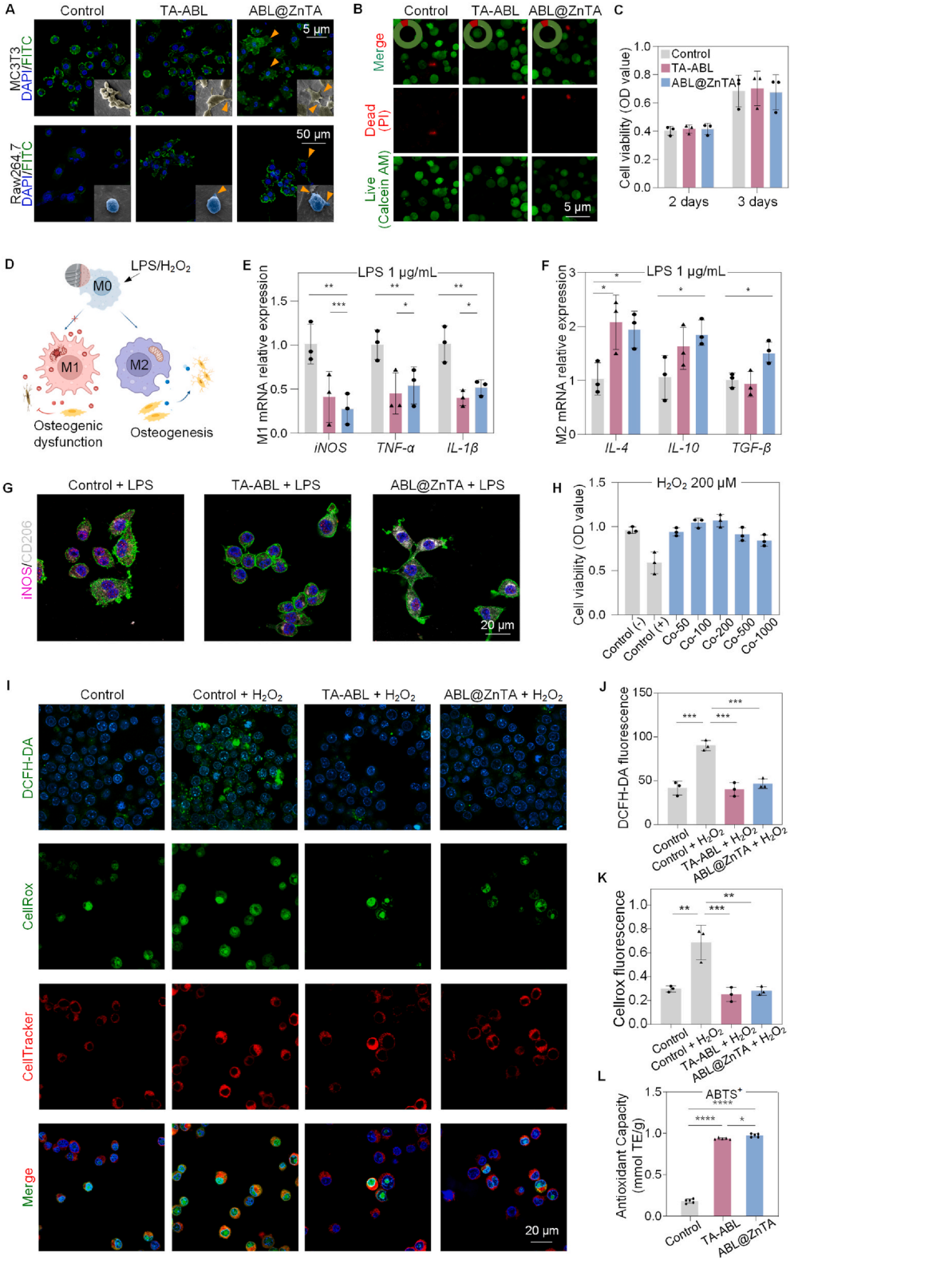

(caption on next page)

Fig. 4. Biocompatibility, anti-inflammatory, and immunomodulatory activity of the ABL@ZnTA nanointerface. (A) CLSM and SEM observation of MC3T3 and RAW264.7 cells morphology seeded on with various coatings for 2 days. Nucleus and cellular actin filaments of cells are labeled with the DAPI (blue) and FITC (green). The arrowheads represent the cellular pseudopodia. For SEM, the MC3T3 cells are pseudo-colored to yellow and RAW264.7 to blue for visual observation. (B) Calcein-AM/PI double staining of RAW264.7 cells for 2 days (Calcein AM-positive cells, green; PI-positive cells, red); semi-quantitative analysis of the proportion of live and dead cells in the top left of images. (C) CCK-8 results of RAW264.7 cells for 2 and 3 days. (D) Schematic diagram of macrophage polarization under LPS/H_2O_2 stimulus and subsequent effect on osteogenesis. (E and F) Relative mRNA expression of M1 and M2-related genes in macrophage under stimulation of 1 μg/mL LPS detected for 2 days by qRT-PCR analysis, n = 3. (G) Immunofluorescence of iNOS and CD206 of macrophage under 1 μg/mL LPS stimulation for 2 days. (H) CCK-8 result of macrophages on the ABL@ZnTA coating of different concentrations stimulated with H_2O_2 (200 μM) for 12 h, n = 3. (I–K) Representative fluorescence images and quantification of DCFH-DA, CellRox, and CellTracker staining for intracellular ROS stimulated with H_2O_2 (200 μM) for 2 h, n = 3. (L) Total antioxidant capacity with ABTS method result of extracellular ROS for 1 day, n = 5. Data are presented as mean ± SD. Statistical significance was calculated *via* one-way ANOVA with Tukey *posthoc* test (*, $P < 0.05$; **, $P < 0.01$; and ***, $P < 0.001$).

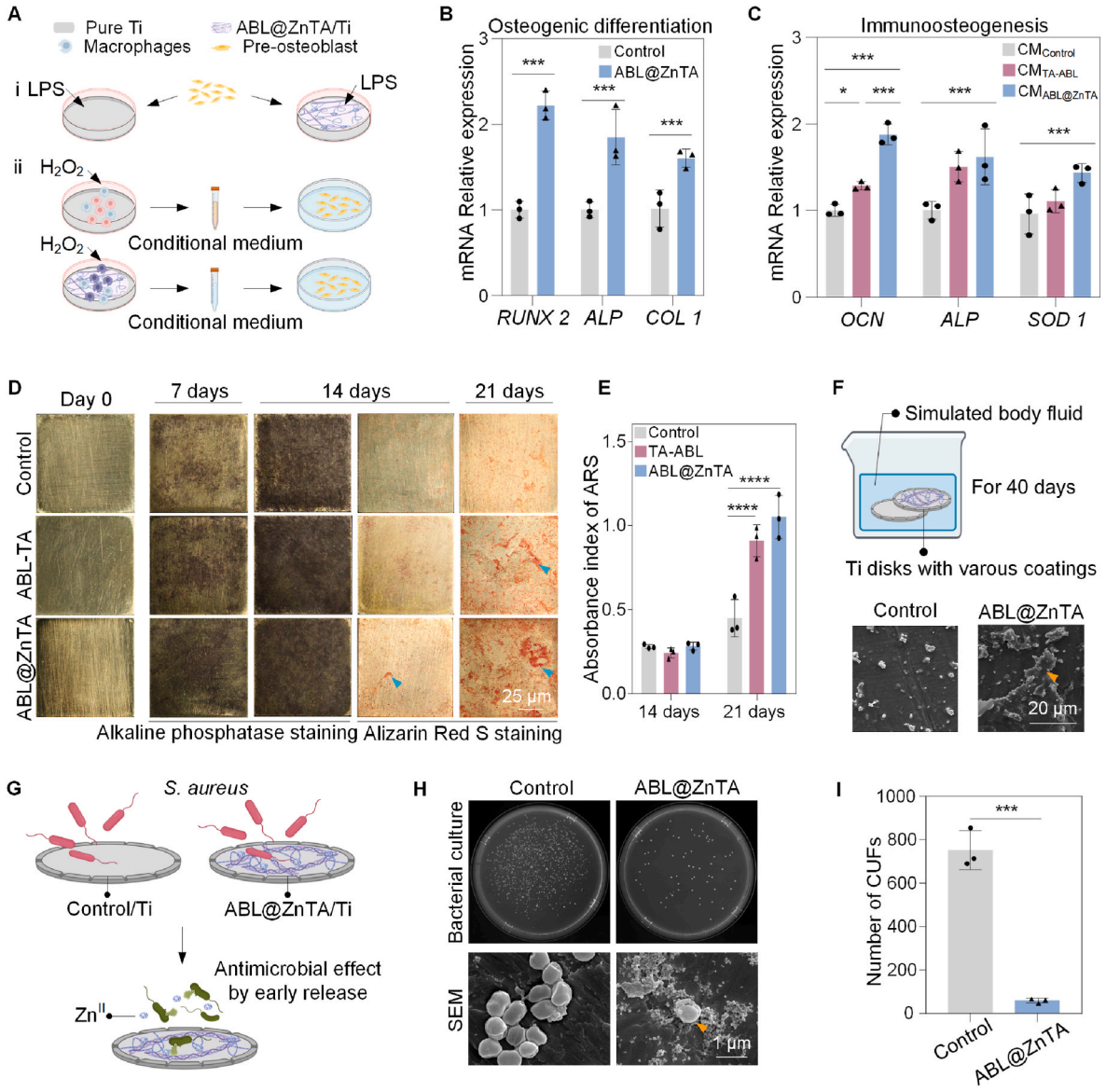

Fig. 5. Enhanced osteogenesis and osteoimmunomodulation of the ABL@ZnTA nanointerface in vitro. (A) Schematic diagram of osteogenic differentiation evaluation under different conditions. Condition i): MC3T3 cells are directly seeded on the different coating samples stimulated with LPS. Condition ii): MC3T3 cells are seeded on the culture plate and incubated in a macrophage-conditioned medium stimulated with H_2O_2. (B) Relative mRNA expression of osteogenesis-related genes encoding *RUNX 2*, *ALP*, and *COL 1* on day 3 with LPS stimulus by qRT-PCR analysis, n = 3. (C) Relative mRNA expression of osteogenesis-related genes encoding *OCN*, *ALP*, and *SOD 1,* detected on day 3 in macrophage-conditioned medium stimulated with H_2O_2 by qRT-PCR analysis, n = 3. The alkaline phosphatase and Alizarin Red S staining images (D) of MC3T3 on various functionalized coating samples at each checkpoint and (E) quantitative analysis of calcium nodules, n = 3. (F) Schematic diagram and SEM of in vitro mineralization of coated Ti soaked in simulated body fluid for 40 days. (G) Schematic diagram of in vitro antibacterial evaluation of coated Ti implants. (H) Top: Representative agar plate images of *S. aureus* after incubation with different samples; Bottom: SEM morphologies of *S. aureus* incubated with different samples (arrowheads indicate the cracked and shrinking membranes). (I) Statistical analysis of colony counts after 24 h of incubation on coated Ti implants, n = 3. Data are presented as mean ± SD. Statistical significance was calculated *via* Student's *t*-test or one-way ANOVA with Tukey *posthoc* test (*, $P < 0.05$; **, $P < 0.01$; and ***, $P < 0.001$).

(*IL-4*), interleukin 10 (*IL-10*), and transforming growth factor-β (*TGF-β*) (Fig. 4E and F). There is no difference in the immunomodulatory effect between the TA-ABL and ABL@ZnTA nanointerfaces. Besides, the immunofluorescence results (Fig. 4G) show that the functional coatings inhibit the M1 phenotype marker iNOS protein expression and promote the M2 phenotype marker CD206 protein expression.

As shown in Fig. 4H, the cell viability is restored by more than 75 % in all ABL@ZnTA coatings of various concentrations, especially the ABL@ZnTA 100 and 200 groups. Combined with previous experimental results, the ABL@ZnTA 100 was used in the following experiments. Besides, as shown in Fig. 4I and J, the nano-coating groups show fluorescence reduction compared with the control group of DCFH-DA. Besides, the TA-ABL and ABL@ZnTA exhibit a drastic scavenging ability on cellular ROS accumulation, with the mean fluorescence intensity of CellRox green staining reduced in half compared to the Control + H_2O_2 group (Fig. 4I and K). In addition, for the micro-environmental ROS scavenging capacity, the Trolox-Equivalent Antioxidant Capacity of the TA-ABL and ABL@ZnTA coatings is higher than that of the control group, near 1 mM (Fig. 4L and Fig. S4). The anti-inflammatory and anti-oxidative stress effects primarily stem from the phenolic hydroxyl groups in polyphenols. Consequently, both TA-ABL and ABL@ZnTA groups demonstrate favorable outcomes in conditions characterized by

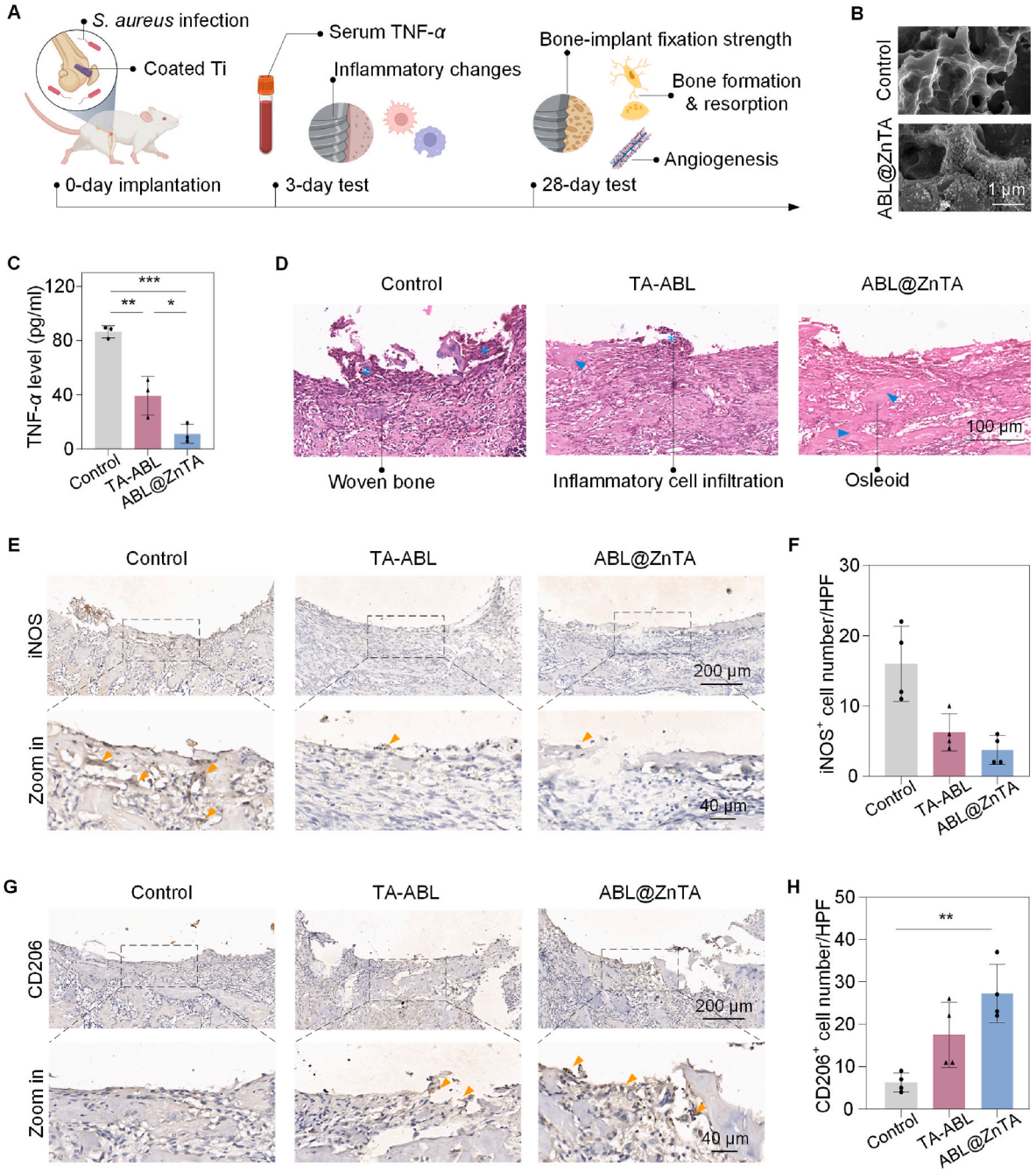

Fig. 6. Early anti-inflammatory and immune modulation of ABL@ZnTA nanointerface in vivo. (A) Schematic illustration of the study timeline. (B) SEM of the sandblasted acid etching Ti implant surface after functionalized modification. (C) Serum TNF-α level at 3 days, n = 3. (D) H&E staining of the peri-implant area at 3 days (asterisks, inflammatory cell infiltrate; arrowheads, newborn osteoid). Immunohistochemistry and semi-quantitative analysis of the positive cell number of M1 marker iNOS (E and F) and M2 marker CD206 (G and H) at 3 days, n = 4 (arrowheads indicate the positive area). Data are presented as mean ± SD. Statistical significance is calculated *via* one-way ANOVA with Tukey *posthoc* test (*, $P < 0.05$; **, $P < 0.01$; and ***, $P < 0.001$).

inflammation or elevated levels of ROS.

3.4. Enhanced osteogenesis and osteoimmunomodulation in vitro

Fig. 5A shows the schematic diagram of osteogenic differentiation in inflammatory or excess oxidative stress conditions. Compared with the control group, the osteoblasts cultured on the ABL@ZnTA group exhibit the highest mRNA levels under LPS-stimulated conditions (Fig. 5B), including runt-related transcription factor 2 (*RUNX 2*), alkaline phosphatase (*ALP*), and collagen type 1 (*COL 1*). To further evaluate the osteoimmune responses and antioxidation of phenolic-peptide coating, MC3T3 cells were seeded in the culture plate and incubated in a macrophage-conditioned medium with H_2O_2. The results confirm that both TA-ABL and ABL@ZnTA coatings show satisfactory immunoosteogenesis effects and antioxygenic properties. Besides, the osteoimmunomodulation capacity is ameliorated when the Zn element is incorporated.

There is almost no visual difference in Ti disks among the samples on day 0. Fig. 5D reveals that ALP expression is darker and denser in the ABL@ZnTA group than in the control group, implying excellent potential for early osteogenic differentiation. After 14 and 21 d of osteogenic differentiation, the control group shows few scattered calcium nodules, while the ABL@ZnTA group displays a significant increase in calcium nodules, which is further validated by the quantitative analysis of alizarin red S (ARS) (Fig. 5E) [55]. SEM result of surface morphology is shown in Fig. 5F and Fig. S5. There is slightly more calcium deposition at 3 d, but evident granular or crumby calcium-phosphate mineralized products are formed at 40 d in the ABL@ZnTA coating.

Fig. 5G shows the diagram of the antibacterial properties of coated Ti implants. The CFUs of *S. aureus* are prominent on LBA plates in the control group. At the same time, the density and colonies of the bacteria decrease dramatically on the ABL@ZnTA surface (Fig. 5H and I). Meanwhile, the morphology of *S. aureus* is presented at the bottom of Fig. 5H. It exhibits a relatively smooth and integrated surface in a uniform spherical shape on the pure Ti disk, while the rough surface with a lot of wrinkles in an irregular shape in the ABL@ZnTA group, indicating that the ABL@ZnTA coating inhibits bacteria growth to some extent *via* contact killing mode.

3.5. Early anti-inflammatory and immune modulation of the ABL@ZnTA nanointerface in bacterial infection microenvironment

We established a femoral bone defect model with *S. aureus* infection (Fig. 6A). The SEM result shows that the coatings can be successfully loaded on the porous surface (Fig. 6B). Bone metabolism spans a lengthy timeline, starting from an early phase of mechanical stability—underscored by initial implant-bone contact and an immediate inflammatory reaction—leading into a prolonged phase of biological stability, marked by the healing and remodeling of bone tissue. Thus, a 28-day observation period is commonly selected to assess long-term stability in rat bone defect and implantation studies. Serum TNF-α levels significantly increased in the control group, were moderately elevated in the TA-ABL group, and were lowest in the ABL@ZnTA group, indicating the early anti-inflammatory effect of the coating. As shown in Fig. 6D of hematoxylin & eosin (H&E) staining, after 3 d of *S. aureus* infection, the peri-implant area is dominated by fibrous tissue, which forms immature woven bone. A large amount of osteoid and immature trabecular bone is evident in the ABL@ZnTA group, and inflammatory cells are rare, indicating the excellent antibacterial and anti-inflammatory effects of TA and Zn^{2+}.

The results show a significant increase in $iNOS^+$ expression in the control group, suggesting an increase in macrophage M1 polarization and a marked inflammatory response around the implant under infected conditions. A few $iNOS^+$ macrophages exist in the TA-ABL group, whereas $iNOS^+$ expression is almost invisible in the ABL@ZnTA group (Fig. 6E and F). Besides, the expression of $CD206^+$ cells is virtually invisible in the control group, indicating very little M2 polarization of macrophages (Fig. 6G and H). A small amount of $CD206^+$ expression is seen in the TA-ABL group. In contrast, $CD206^+$ expression significantly increases in the ABL@ZnTA group, presumably due to the synergistic effect of TA and Zn, resulting in the phenotypic transformation of macrophages.

3.6. Enhanced osseointegration strength and osteogenesis promotion in bacterial infection microenvironment

Fig. 7A displays the representative load-displacement curves and corresponding average maximum push-out force (Fmax). After functional modification, however, the Fmax of ABL@ZnTA increases sharply to 28.52 ± 4.63 N, much higher than those of the control (4.93 ± 1.42 N) and TA-ABL (13.48 ± 7.36 N) groups. According to the SEM analysis, the regenerated bone tissue has permeated the implants, as indicated by some micropores filling with the new bone tissues. The porous structure is visible around the control implant, suggesting less bone tissue covering the surface and explaining why implants in the control group are more accessible to push out. The newly formed bone tissue surrounding the TA-ABL and ABL@ZnTA implants is drastically more extensive and denser, but the latter is almost wrapped with more regular and thicker freshly formed bone tissues. EDS mapping results show phosphorus deposits on the TA-ABL surface, while the ABL@ZnTA coating exhibits a significant increase in both calcium and phosphorus, suggesting extensive calcified matrix development.

The regenerated bone quality and quantity around the implants 28 d after implantation were reconstructed and analyzed through Micro-CT. Larger bone volume and a higher bone-implant contact area are found around the TA-ABL and ABL@ZnTA nanointerfaces (Fig. 7C). The quantitative Micro-CT analysis coupled with corresponding images of new trabecular bone exhibits that the trabecular bone number (Tb.N) and trabecular bone thickness (Tb.Th) increase in both coated implants (Fig. 7D and Fig. S6). To analyze the osseointegration further, hard tissue section staining of Methylene blue magenta was operated on in our study. In Fig. 7E, a thin new tissue layer around the implant is displayed in the control group. More uniform and continuous new bone is found and tightly connected with the modified implants, especially for the ABL@ZnTA implants.

Fig. 7F shows some fibrous tissue and sparse bone trabeculae around the bone-implant interface in the control group, while a small amount of woven bone is observed in the TA-ABL group. In the ABL@ZnTA group, there is a significant increase of lamellar bone tightly integrated onto the coated implant, with bone trabeculae structurally regular and aligned, and abundant neovascularization is observed. This was further verified by Masson's Trichrome staining (Fig. 7G and H) [56], which shows that most of the control group is aged bone tissue (stained red), probably due to infection and inflammation. In the ABL@ZnTA group, the network of collagen fibers is evident, and there is a significant increase in new bone formation (stained blue). The bottom of Fig. 7G and I shows significantly higher expression in the ABL@ZnTA group than the control group, indicating higher osteogenic activity and appealing osseointegration of functional coating. As shown in Fig. S7, there is no significant difference in the number of $TRAP^+$ osteoclasts at the peri-implant or periphery periosteum, suggesting that the coating does not affect osteoclastic activity. In addition, H&E staining of the internal organs shows no statistical difference (Fig. S8).

4. Discussion

We developed a multifunctional implant nanocoating through the engineering of an integrative peptide-metal-phenolic network inspired by the structure of the zinc finger motif. The potential advantage of the nanointerface is the versatility to modify various implants made from metals, ceramics, and polymers [57]. To understand the bonding mechanisms of the phenolic-peptide network, TA molecules coordinate

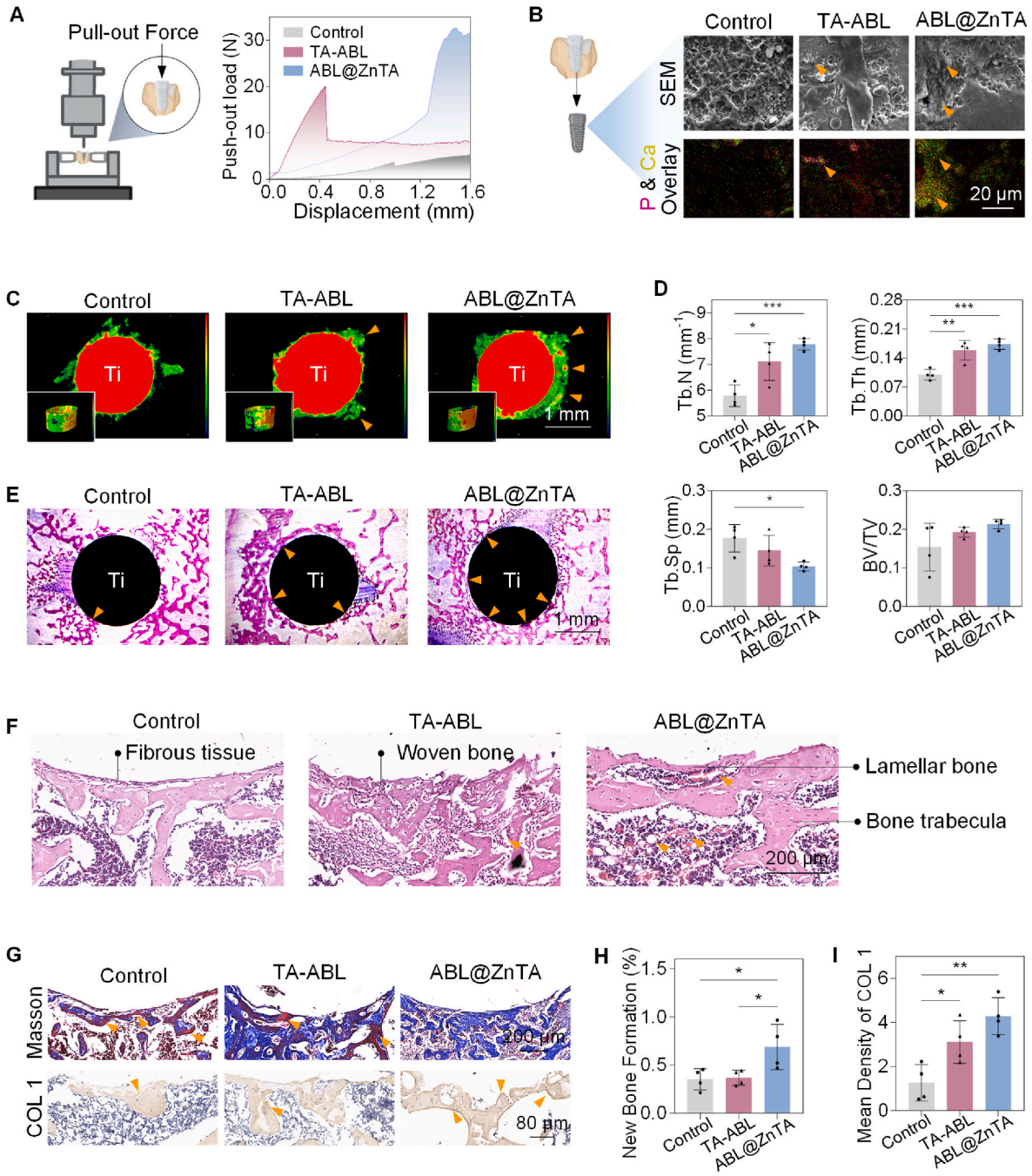

Fig. 7. Enhanced osseointegration strength and osteogenesis promotion in the long term. (A) Schematic diagram of the biomechanical push-out test and load-displacement curves of the implants at 28 days, n = 3. (B) Representative images of new bone tissue attachment to the implant interface at 28 days by SEM and EDS mapping (arrowheads indicate the calcified tissue). (C) Representative images of the three-dimensional reconstructed Micro-CT images and Tb.Th of newborn bone at 28 days (arrowheads indicate the new bone formation). (D) Quantitative analysis of Micro-CT data including Tb.N, Tb.Th, Tb.Sp, and BV/TV, n = 4. (E) Bone-implant interface by hard tissue sections stained with Methylene blue magenta (arrowheads indicate new bone in direct contact with the implant). (F) Histological examination of H&E staining (arrowheads indicate the new blood vessels in the peri-implant area). (G) Evaluation of osteogenic differentiation by Masson's Trichrome staining (blue, new bone, labeled by yellow arrowheads; red, mature bone); and immunohistochemistry of osteogenic marker (arrowheads indicate the positive area of COL 1), and corresponding semi-quantitative analysis, n = 4 (H and I). Data are presented as mean ± SD. Statistical significance was calculated *via* one-way ANOVA with Tukey *posthoc* test (*, $P < 0.05$; **, $P < 0.01$; and ***, $P < 0.001$).

with Zn^{II} ions to form a metal-phenolic supramolecular network due to abundant galloyl groups [58]. Two galloyl groups from TA can react with each central Zn^{II} to create a stable octahedral complex. This allows each TA molecule to react with several Zn^{II} centers to anchor the second-generation anabolic drug for treating osteoporosis, ABL. The ABL@ZnTA nanointerface is mainly formed by reversible and non-covalent interaction in self-assembly, which is conducive to maintaining the bioactivity and stability of ABL.

The mechanical properties of MPN generally range between 3 and 10 Gpa [59]. In the ABL@ZnTA system, MPN demonstrates the capability to form a comparatively more robust network than that achieved through traditional layer deposition modification techniques [60]. This underscores its potential to resist frictional forces encountered during the implantation process, particularly in the implantation of dental implants

or orthodontic microscrews.

Implant-associated infections contribute to chronic inflammation and increased risk of implant failure due to mixed pro/anti-inflammatory responses and microbial contamination [61,62]. Besides, bacterial phagocytosis can continuously activate the immune response and M1-type macrophages, which affects osteogenesis [63,64]. Macrophages are essential in the early inflammatory response but can remain in a prolonged 'frustrated phagocytosis' state, unable to resolve the chronic inflammation effectively [65]. The result proves that the ABL@ZnTA coating exhibits excellent performance in the immunomodulation of macrophage phenotype, osteogenic differentiation, and inhibition of pathogenic bacterial growth during the perioperatively.

Device-associated infections result from bacterial adherence and subsequent biofilm formation at the implant site [66]. Preventing bacterial attachment and proliferation on implants during the perioperative period is crucial to ensure successful implantation in the short term [67]. The antibacterial effectiveness of ABL@ZnTA surfaces was specifically assessed against *S. aureus* due to its common association with Gram-positive staphylococcal infections, particularly in surgical trauma repair scenarios [68,69]. Zinc ions bind to bacterial enzymes' active sites, modifying their structures and hindering pathogen functions [70]. Acidic conditions weaken metal-phenolic interactions, causing zinc dissociation [71]. In the mildly acidic environment of infections (pH = 4.5−6.5), due to bacterial metabolism and the host's immune response, early zinc release from the metal-phenolic network enhances antibacterial activity in the initial stages.

Intermittent administration of TPTD has been shown to enhance bone density, yet its continuous and excessive presence results in bone resorption [72]. This biphasic effect of parathyroid hormone analogs is influenced by the interaction dynamics with varying states of its receptor (PTH-PTH1R) and dosing regimen [73]. Despite its inherent instability, PTHrP fosters bone regeneration while inducing lower levels of bone resorption and less pronounced hypercalcemic effects than TPTD, primarily due to its quicker dissociation of PTHrP-PTH1R than PTH-PTH1R [74]. In pursuit of augmenting the stability of TPTD and PTHrP, researchers have synthesized the ABL peptides, effectively extending the anabolic window and mitigating the hypercalcemic tendencies. Besides, the daily release does not exceed 4 μg/mL over the initial 3 days, ensuring that no marked osteoclastic activity is induced, even in the early stages [75]. It may be due to the excellent slow-release effect, releasing peptide microdose in the local area, providing a guarantee for long-term osteogenesis without stimulating bone resorption, and co-constructing bone homeostatic equilibrium.

5. Conclusion

In summary, we have innovated a zinc finger-inspired MPN-based nanointerface at the bone-implant interface, designated as ABL@ZnTA. This multifunctional nanocoating, constructed by natural polyphenols, osteogenic peptide ABL, and Zn^{2+} ions, establishes a new paradigm of nanotechnology for implant surface functionalization. The ABL@ZnTA nanocoating not only ensures the stability of the ABL peptides through robust multiple molecular interactions with phenolic groups but also leverages the coordinated Zn^{II} to mimic the Zn finger motif. The ABL@ZnTA nanointerface has shown promising performance in the enhancement of bone-implant osseointegration within a challenging bacterial infection microenvironment. More importantly, ABL@ZnTA successfully overcomes the great difficulty in balancing inflammation mitigation and immunomodulation, thus creating a synergistic and balancing strategy for implant infection defense and osteogenesis promotion for early internal fixation of traumatic fractures and immediate dental implantation.

Conflict of interest

The authors declare that they have no known competing financial interests or personal relationships that could have appeared to influence the work reported in this paper.

6. Ethics approval and consent to participate

The animal experiments were approved by the Research Ethics Committee of West China Hospital of Stomatology, Sichuan University, China (No. WCHSIRB-D-2023-362) and performed by the guidelines for animal experimentation of the university/the Animal Research N3CRs guidelines for Reporting of In Vivo Experiments (ARRIVE) guidelines.

Data availability statement

The data that support the findings of this study are available from the corresponding author upon reasonable request.

CRediT authorship contribution statement

Lin Xu: Writing – original draft, Methodology, Investigation, Data curation, Conceptualization. **Jie Fang:** Writing – original draft, Methodology, Funding acquisition, Data curation, Conceptualization. **Jiezhou Pan:** Software, Methodology, Investigation. **Hexu Qi:** Software, Methodology, Investigation. **Yun Yin:** Software, Methodology, Investigation. **Yunxiang He:** Software, Methodology, Investigation. **Xueqi Gan:** Supervision, Methodology. **Yifei Li:** Writing – review & editing, Supervision, Funding acquisition. **Yu Li:** Writing – review & editing, Supervision, Funding acquisition. **Junling Guo:** Writing – review & editing, Supervision, Funding acquisition, Conceptualization.

Declaration of competing interest

The authors declare that they have no known competing financial interests or personal relationships that could have appeared to influence the work reported in this paper.

Acknowledgments

This work was supported by the National Natural Science Foundation of China (J.F., Grant no. 32000928), Sichuan Science and Technology Program (J.F., Grant no. 2023YFS0150), the National Natural Science Foundation of China (Y.L., Grant no. 82270249), the National Key R&D Program of China (J.G., Grant No. 2022YFA0912800), the National Natural Science Foundation of China (J.G., Grant No. 22178233), the National Excellent Young Scientist Fund (J.G., Grant No. 00308054A1045), Sichuan Tianfu Emei Project (J.G., Grant No. 2022-EC02-00073-CG), the Talents Program of Sichuan Province (J.G.), the Double First Class University Plan of Sichuan University (J.G.), the State Key Laboratory of Polymer Materials Engineering (J.G., Grant No. sklpme 2020-03-01), the National Natural Science Foundation of China (Y.L., Grant no. 31971247, 82371003).

Appendix A. Supplementary data

Supplementary data to this article can be found online at https://doi.org/10.1016/j.bioactmat.2024.08.009.

References

[1] W.J. Metsemakers, M. Morgenstern, E. Senneville, et al., General treatment principles for fracture-related infection: Recommendations from an international expert group, Arch. Orthop. Traum. Su. 140 (8) (2020) 1013–1027.
[2] W.J. Metsemakers, J. Onsea, E. Neutjens, et al., Prevention of fracture-related infection: a multidisciplinary care package, Int. Orthop. 41 (12) (2017) 2457–2469.
[3] M. Rupp, D. Popp, V. Alt, Prevention of infection in open fractures: where are the pendulums now? Injury 51 (Suppl 2) (2020) S57–S63.

[4] C. Mauffrey, M.E. Hake, V. Chadayammuri, et al., Reconstruction of long bone infections using the induced membrane technique: tips and tricks, J. Orthop. Trauma 30 (6) (2016) e188–e193.
[5] A.O. Salgado-Peralvo, J.F. Pena-Cardelles, N. Kewalramani, et al., Preventive antibiotic therapy in the placement of immediate implants: a systematic review, J. Antibiot. 11 (1) (2021) 5.
[6] D. Zhao, Y. Wu, C. Xu, et al., Immediate dental implant placement into infected vs. Non-infected sockets: a meta-analysis, Clin. Oral Implants Res. 27 (10) (2016) 1290–1296.
[7] O.B. de Oliveira-Neto, C.A. Lemos, F.T. Barbosa, et al., Immediate dental implants placed into infected sites present a higher risk of failure than immediate dental implants placed into non-infected sites: systematic review and meta-analysis, Med. Oral Patol. Oral Cir. Bucal 24 (4) (2019) e518–e528.
[8] O.D. Umeh, U.L. Offojebe, I.G. Isiekwe, et al., Survival analysis of temporary anchorage devices: a retrospective analysis in a Nigerian orthodontic patient population, J. Orthod. Sci. 12 (2023) 45.
[9] Y. Wu, H. Wang, P.K. Chu, Enhancing macrophages to combat intracellular bacteria, Innov. Life 1 (2) (2023) 100027.
[10] H. Wei, J. Cui, K. Lin, et al., Recent advances in smart stimuli-responsive biomaterials for bone therapeutics and regeneration, Bone Research 10 (1) (2022) 17.
[11] J. Zhang, Y. Zhuang, R. Sheng, et al., Smart stimuli-responsive strategies for titanium implant functionalization in bone regeneration and therapeutics, Mater. Horiz. 11 (1) (2024) 12–36.
[12] J. Zeng, C. Gu, X. Geng, et al., Combined photothermal and sonodynamic therapy using a 2d black phosphorus nanosheets loaded coating for efficient bacterial inhibition and bone-implant integration, Biomaterials 297 (2023) 122122.
[13] S. Zhang, H. Yang, M. Wang, et al., Immunomodulatory biomaterials against bacterial infections: progress, challenges, and future perspectives, Innovation 4 (6) (2023) 100503.
[14] M.U. Joshi, S.P. Kulkarni, M. Choppadandi, et al., Current state of art smart coatings for orthopedic implants: a comprehensive review, Smart Mater. Med. 4 (2023) 661–679.
[15] J. Li, X. Jiang, H. Li, et al., Tailoring materials for modulation of macrophage fate, Adv. Mater. 33 (12) (2021) e2004172.
[16] H. Newman, Y.V. Shih, S. Varghese, Resolution of inflammation in bone regeneration: from understandings to therapeutic applications, Biomaterials 277 (2021) 121114.
[17] N. Su, C. Villicana, F. Yang, Immunomodulatory strategies for bone regeneration: a review from the perspective of disease types, Biomaterials 286 (2022) 121604.
[18] P. Yousefpour, K. Ni, D.J. Irvine, Targeted modulation of immune cells and tissues using engineered biomaterials, Nat. Rev. Bioeng. 1 (2) (2023) 107–124.
[19] S. Amin Yavari, S.M. Castenmiller, J.A.G. van Strijp, et al., Combating implant infections: shifting focus from bacteria to host, Adv. Mater. 32 (43) (2020) e2002962.
[20] F. Jin, M. Liu, D. Zhang, et al., Translational perspective on bone-derived cytokines in inter-organ communications, Innovation 4 (1) (2023) 100365.
[21] Y. Xu, Y. Li, A. Gao, et al., Gasotransmitter delivery for bone diseases and regeneration, The Innovation Life 1 (1) (2023) 100015.
[22] H. De Bruyn, S. Raes, P.O. Ostman, et al., Immediate loading in partially and completely edentulous jaws: a review of the literature with clinical guidelines, Periodontol 2000 66 (1) (2014) 153–187.
[23] R. Chen, J. Wang, C. Liu, Biomaterials act as enhancers of growth factors in bone regeneration, Adv. Funct. Mater. 26 (48) (2016) 8810–8823.
[24] Z. Zhao, D.C. Pan, Q.M. Qi, et al., Engineering of living cells with polyphenol-functionalized biologically active nanocomplexes, Adv. Mater. 32 (49) (2020) e2003492.
[25] Y. Wang, X. Lu, X. Wu, et al., Chemically modified DNA nanostructures for drug delivery, Innovation 3 (2) (2022) 100217.
[26] R.M. Neer, C.D. Arnaud, J.R. Zanchetta, et al., Effect of parathyroid hormone (1−34) on fractures and bone mineral density in postmenopausal women with osteoporosis, N. Engl. J. Med. 344 (19) (2001) 1434–1441.
[27] P. Lyu, B. Li, P. Li, et al., Parathyroid hormone 1 receptor signaling in dental mesenchymal stem cells: basic and clinical implications, Front. Cell Dev. Biol. 9 (2021) 654715.
[28] J. Tang, D. Yan, L. Chen, et al., Enhancement of local bone formation on titanium implants in osteoporotic rats by biomimetic multilayered structures containing parathyroid hormone (PTH) related protein, Biomed. Mater. 15 (4) (2020) 045011.
[29] M.N. Handel, I. Cardoso, C. von Bulow, et al., Fracture risk reduction and safety by osteoporosis treatment compared with placebo or active comparator in postmenopausal women: systematic review, network meta-analysis, and meta-regression analysis of randomised clinical trials, BMJ 381 (2023) e068033.
[30] T. Chen, Y. Wang, Z. Hao, et al., Parathyroid hormone and its related peptides in bone metabolism, Biochem. Pharmacol. 192 (2021) 114669.
[31] M. Hiligsmann, S.A. Williams, L.A. Fitzpatrick, et al., Cost-effectiveness of sequential treatment with abaloparatide vs. teriparatide for United States women at increased risk of fracture, Semin. Arthritis Rheum. (2019) 184–196. Elsevier.
[32] P.D. Miller, G. Hattersley, B.J. Riis, et al., Effect of abaloparatide vs placebo on new vertebral fractures in postmenopausal women with osteoporosis: a randomized clinical trial, JAMA 316 (7) (2016) 722–733.
[33] Y. Li, Y. Qian, H. Qiao, et al., Abaloparatide outperforms teriparatide in protecting against alveolar bone loss in experimental periodontitis, J. Periodontol. 94 (2) (2023) 244–255.
[34] B. Tan, Y. Wu, R. Wang, et al., Biodegradable nanoflowers with abaloparatide spatiotemporal management of functional alveolar bone regeneration, Nano Lett. 24 (8) (2024) 2619–2628.
[35] J. Satterwhite, M. Heathman, P.D. Miller, et al., Pharmacokinetics of teriparatide (rhPTH [1–34]) and calcium pharmacodynamics in postmenopausal women with osteoporosis, Calcif. Tissue Int. 87 (2010) 485–492.
[36] J. Guo, Y. Ping, H. Ejima, et al., Engineering multifunctional capsules through the assembly of metal-phenolic networks, Angew. Chem. Int. Ed. Engl. 53 (22) (2014) 5546–5551.
[37] H. Ejima, J.J. Richardson, K. Liang, et al., One-step assembly of coordination complexes for versatile film and particle engineering, Science 341 (6142) (2013) 154–157.
[38] Y. Zhang, J. Wang, Y. He, et al., Customizable supraparticles constructed from catechol-terminated molecular building blocks with controllable intermolecular interactions, Angew. Chem. Int. Ed. Engl. 62 (29) (2023) e202303463.
[39] Y. Wang, Y. He, Q. Wang, et al., Microporous membranes for ultrafast and energy-efficient removal of antibiotics through polyphenol-mediated nanointerfaces, Matter 6 (1) (2023) 260–273.
[40] X. Qiu, X. Wang, Y. He, et al., Superstructured mesocrystals through multiple inherent molecular interactions for highly reversible sodium ion batteries, Sci. Adv. 7 (37) (2021) eabh3482.
[41] Y. Han, Z. Lin, J. Zhou, et al., Polyphenol-mediated assembly of proteins for engineering functional materials, Angew. Chem. Int. Ed. Engl. 59 (36) (2020) 15618–15625.
[42] Y. Guo, Q. Sun, F.G. Wu, et al., Polyphenol-containing nanoparticles: synthesis, properties, and therapeutic delivery, Adv. Mater. 33 (22) (2021) e2007356.
[43] X. Yan, Z. Zeng, D.J. McClements, et al., A review of the structure, function, and application of plant-based protein-phenolic conjugates and complexes, Compr. Rev. Food Sci. Food Saf. 22 (2) (2023) 1312–1336.
[44] M. Fu, P.J. Blackshear, RNA-binding proteins in immune regulation: a focus on CCCH zinc finger proteins, Nat. Rev. Immunol. 17 (2) (2017) 130–143.
[45] Y. Han, R.P.M. Lafleur, J. Zhou, et al., Role of molecular interactions in supramolecular polypeptide-polyphenol networks for engineering functional materials, J. Am. Chem. Soc. 144 (27) (2022) 12510–12519.
[46] Y. Han, J. Zhou, Y. Hu, et al., Polyphenol-based nanoparticles for intracellular protein delivery via competing supramolecular interactions, ACS Nano 14 (10) (2020) 12972–12981.
[47] Q. Zhang, Y. Yang, D. Suo, et al., A biomimetic adhesive and robust Janus patch with anti-oxidative, anti-inflammatory, and anti-bacterial activities for tendon repair, ACS Nano 17 (17) (2023) 16798–16816.
[48] Y. Ju, H. Liao, J.J. Richardson, et al., Nanostructured particles assembled from natural building blocks for advanced therapies, Chem. Soc. Rev. 51 (11) (2022) 4287–4336.
[49] J. Pan, G. Gong, Q. Wang, et al., A single-cell nanocoating of probiotics for enhanced amelioration of antibiotic-associated diarrhea, Nat. Commun. 13 (1) (2022) 2117.
[50] Q. Liu, Y. He, Y. Fang, et al., Emerging self-assembled nanoparticles constructed from natural polyphenols for intestinal diseases, Adv. Nanobiomed. Res. 3 (2023) 2300046.
[51] M. Shin, H.A. Lee, M. Lee, et al., Targeting protein and peptide therapeutics to the heart via tannic acid modification, Nat. Biomed. Eng. 2 (5) (2018) 304–317.
[52] M. Cicciu, G. Cervino, D. Milone, et al., FEM analysis of dental implant-abutment interface overdenture components and parametric evaluation of equator((r)) and locator((r)) prosthodontics attachments, Materials 12 (4) (2019) 1–13.
[53] A. Simchi, E. Tamjid, F. Pishbin, et al., Recent progress in inorganic and composite coatings with bactericidal capability for orthopaedic applications, Nanomedicine 7 (1) (2011) 22–39.
[54] H. Puchtler, S.N. Meloan, M.S. Terry, On the history and mechanism of alizarin and alizarin red s stains for calcium, J. Histochem. Cytochem. 17 (2) (1969) 110–124.
[55] C. Rentsch, W. Schneiders, S. Manthey, et al., Comprehensive histological evaluation of bone implants, Biomatter 4 (1) (2014) e27993.
[56] P. Chanphai, H. Tajmir-Riahi, Tea polyphenols bind serum albumins: a potential application for polyphenol delivery, Food Hydrocoll 89 (2019) 461–467.
[57] H. Fan, J. Wang, Q. Zhang, et al., Tannic acid-based multifunctional hydrogels with facile adjustable adhesion and cohesion contributed by polyphenol supramolecular chemistry, ACS Omega 2 (10) (2017) 6668–6676.
[58] G. Yun, J.J. Richardson, M. Biviano, et al., Tuning the mechanical behavior of metal-phenolic networks through building block composition, ACS Appl. Mater. Interfaces 11 (6) (2019) 6404–6410.
[59] A. Sarode, A. Annapragada, J. Guo, et al., Layered self-assemblies for controlled drug delivery: a translational overview, Biomaterials 242 (2020) 119929.
[60] Y. Ding, R. Ma, G. Liu, et al., Fabrication of a new hyaluronic acid/gelatin nanocomposite hydrogel coating on titanium-based implants for treating biofilm infection and excessive inflammatory response, ACS Appl. Mater. Interfaces 15 (10) (2023) 13783–13801.
[61] J. Kzhyshkowska, A. Gudima, V. Riabov, et al., Macrophage responses to implants: prospects for personalized medicine, J. Leukoc. Biol. 98 (6) (2015) 953–962.
[62] L. Lang, Y. Zhang, A. Yang, et al., Macrophage polarization induced by quinolone antibiotics at environmental residue level, Int. Immunopharmacol. 106 (2022) 108596.
[63] I.M. Castano, R.M. Raftery, G. Chen, et al., Rapid bone repair with the recruitment of CD206(+)M2-like macrophages using non-viral scaffold-mediated miR-133a inhibition of host cells, Acta Biomater. 109 (2020) 267–279.
[64] E.M. O'Brien, G.E. Risser, K.L. Spiller, Sequential drug delivery to modulate macrophage behavior and enhance implant integration, Adv. Drug Deliv. Rev. 149–150 (2019) 85–94.
[65] E.M. Hetrick, M.H. Schoenfisch, Reducing implant-related infections: active release strategies, Chem. Soc. Rev. 35 (9) (2006) 780–789.

[66] J. Min, K.Y. Choi, E.C. Dreaden, et al., Designer dual therapy nanolayered implant coatings eradicate biofilms and accelerate bone tissue repair, ACS Nano 10 (4) (2016) 4441–4450.
[67] W.F. Oliveira, P.M.S. Silva, R.C.S. Silva, et al., Staphylococcus aureus and staphylococcus epidermidis infections on implants, J. Hosp. Infect. 98 (2) (2018) 111–117.
[68] W. Zimmerli, P. Sendi, Pathogenesis of implant-associated infection: the role of the host, Semin. Immunopathol. 33 (3) (2011) 295–306.
[69] S.H. Cha, J. Hong, M. McGuffie, et al., Shape-dependent biomimetic inhibition of enzyme by nanoparticles and their antibacterial activity, ACS Nano 9 (9) (2015) 9097–9105.
[70] X. Liao, G. Gong, M. Dai, et al., Systemic tumor suppression via macrophage-driven automated homing of metal-phenolic-gated nanosponges for metastatic melanoma, Adv. Sci. 10 (18) (2023) e2207488.
[71] X. Cheng, X. Pei, W. Xie, et al., pH-triggered size-tunable silver nanoparticles: targeted aggregation for effective bacterial infection therapy, Small 18 (22) (2022) e2200915.
[72] G. Tabacco, J.P. Bilezikian, Osteoanabolic and dual action drugs, Br. J. Clin. Pharmacol. 85 (6) (2019) 1084–1094.
[73] S. Bhattacharyya, S. Pal, N. Chattopadhyay, Abaloparatide, the second generation osteoanabolic drug: molecular mechanisms underlying its advantages over the first-in-class teriparatide, Biochem. Pharmacol. 166 (2019) 185–191.
[74] R.C. Gensure, T.J. Gardella, H. Jüppner, Multiple sites of contact between the carboxyl-terminal binding domain of PTHrP-(1–36) analogs and the amino-terminal extracellular domain of the PTH/PTHrP receptor identified by photoaffinity cross-linking, J. Biol. Chem. 276 (31) (2001) 28650–28658.
[75] A. Makino, H. Takagi, Y. Takahashi, et al., Abaloparatide exerts bone anabolic effects with less stimulation of bone resorption-related factors: a comparison with teriparatide, Calcif, Tissue Int. 103 (3) (2018) 289–297.